Journal of 先进陶瓷 ISSN 2226-4108 CN 10-1154/TQ Advanced Ceramics
清华大学出版社 Tsinghua University Press
SciOpen

J Adv Ceram 2026, **15**: 9221376

https://doi.org/10.26599/JAC.2026.9221376

Research Article

Defect-engineered high-entropy spinel ferrite nanofibers via Joule heating for superior microwave absorption

Haiming Li [1,†], Yuhang Bai [2,†], Ziying Feng [2], Dan Luo [1], Yudong Gao [1], Zexian Xu [1,3,*]

[1] *The Affiliated Hospital of Qingdao University, Qingdao 266003, China*
[2] *School of Material Science and Engineering, Xi'an University of Science and Technology, Xi'an 710054, China*
[3] *Dental Digital Medicine & 3D Printing Engineering Laboratory of Qingdao, Qingdao 266003, China*
† *These authors contributed equally to this work.*

* Corresponding author.
E-mail: xuzexian@qdu.edu.cn

Received: June 29, 2026; Revised: August 22, 2026; Accepted: September 9, 2026

清华大学出版社 Tsinghua University Press | SciOpen

Abstract: Spinel ferrites with exceptional magnetic permeability, optimal impedance matching, and robust chemical stability have attracted considerable attention in high-performance electromagnetic wave (EMW) absorption applications, yet their insufficient dielectric dissipation and constrained absorption bandwidth limit their advanced EMW absorption uses. Herein, an entropy-driven strategy based on electrospinning and ultrafast Joule-heating method was designed to fabricate novel defect-

rich $(Mn_{0.2}Co_{0.2}Ni_{0.2}Cu_{0.2}Zn_{0.2})Fe_2O_4$ high-entropy spinel ferrite nanofibers (HESF NFs). The results demonstrate that high configurational entropy of HESF NFs induces severe lattice distortions, abundant oxygen vacancies, and ultra-dense grain boundaries, significantly reinforcing dipole and interfacial polarization. The inherent conductive dissipation in the 3D fibrous architecture and multiscale EMW scattering concurrently refine the impedance matching. The quantitative analysis suggests that the entropy-mediated lattice strain and oxygen vacancies govern charge redistribution. The density functional theory (DFT) calculations attribute the enhanced dielectric loss to bandgap narrowing and localized electronic states. All these features endow the resultant HESF NFs with advanced EMW performance, achieving a minimum reflection loss of -53.58 dB at 1.6 mm and an effective absorption bandwidth of 7.82 GHz at 2.03 mm. Overall, defect density plays a critical role in modulating EMW dissipation through Joule-heating technology, and should be the focus for designing high-performance EMW absorbers-based HESF NFs.

Keywords: Joule-heating; High-entropy oxides; Nanofiber; Structural defects; Microwave absorption

1 Introduction

The synergistic convergence of fifth-generation (5G) communication technology with the Internet of Things (IoT) has engendered the development of various wireless electronic devices with unprecedented electromagnetic complexities and a threat to both biological health and ecological security due to the high-frequency emitted electromagnetic waves (EMW) [1-2]. Such electromagnetic pollution can be solved by engineering advanced EMW-absorbing materials endowed with exceptional broadband absorption efficiency combined with lightweight and thin-thickness architectures [3-4]. Among materials, spinel ferrites have shown promise as high-performance EMW absorbers due to their superior magnetic permeability, excellent impedance

matching characteristics, remarkable chemical stability, and cost-effectiveness [5]. However, their insufficient dielectric loss and narrow absorption bandwidth significantly constrain their practical applications in advanced anti-electromagnetic interference systems [6]. This can be overcome through various modification strategies, predominantly employing composite approaches based on carbon materials and conductive polymers to form intricate heterostructures [7-10]. Nevertheless, despite the efficacy of these composites in enhancing dielectric loss, their cumbersome fabrication protocols and compromised structural stability limit their further applications. Alternatively, research efforts are being reoriented toward modulating the intrinsic characteristics of materials to concurrently streamline manufacturing processes and achieve performance breakthroughs.

One way to achieve this is through revolutionary design of materials, among which high-entropy (HE) composites have received increasing attention owing to their simple solid-solution structures comprising multiple principal elements (typically ≥5) in near-equimolar ratios [11]. Such advanced systems harness multi-principal-element synergy, lattice distortion, and high configurational entropy effects, allowing them to unlock unprecedented functionalities in EMW absorption [12-14]. For instance, metal vacancy could induce dipole polarization loss, conductive loss, and nanocluster-triggered interfacial polarization loss in HE diborides prepared via boron thermal reduction, synergistically endowing $(HfTaVWTiMoNbZrCo)B_2$ with exceptional microwave absorption, achieving a minimum reflection loss (RL_{min}) of -42.6 dB at 1.5 mm thickness combined with an effective absorption bandwidth (EAB) of 7.2 GHz (10.86-17.32 GHz) [15]. Similarly, abundant structural defects and optimized morphology in HE transition-metal carbide $(V_{0.25}Ti_{0.25}Cr_{0.25}Mo_{0.25})_2GaC$ fabricated through solid-state reaction could generate remarkable dipole/interface polarization, multiple reflections, and scattering, achieving an RL_{min} of -47.12 dB at 2.06 mm (12.13 GHz) combined with a broad EAB of 4.56 GHz (9.92-14.48 GHz) at 2.03 mm [16]. Therefore, implementing HE engineering in ferrites would promote lattice distortion and oxygen vacancy formation through multi-principal entropy enhancement effects. Concurrently, the stochastic

distribution of multiple elements may induce nanodomain architectures and electron-hopping resonance, establishing multi-relaxation polarization mechanisms allowing effective mitigation of the inadequate dielectric loss characteristic of conventional ferrites [17]. However, most research and development in this area have so far focused on micron-scale high-entropy spinel ferrite (HESF) particles, which are limited by two main aspects. The first is the constrained specific surface area and suboptimal EMW propagation pathways, and the second is the intrinsic isotropic nature, merely enabling disordered multiple reflections. Alternatively, one-dimensional nanofibers (1D NFs) with high aspect ratios enable the construction of three-dimensional (3D) conductive networks with pronounced anisotropic electromagnetic responses [18-20]. Such unique architectures facilitate the formation of multiscale heterogeneous interfaces, prolonging EMW propagation paths through optimized multiple scattering effects for enhanced energy dissipation. Additionally, the substantial specific surface area provides abundant surface dangling bonds acting as intensified polarization centers for reinforced dielectric loss. These synergistic advantages endow nanofiber-structured HESF with advanced EMW absorption performance through multiple loss mechanisms, surpassing their particulate counterparts.

The conventional synthesis of ferrite predominantly relies on high-temperature solid-state reactions, in which the sluggish heating/cooling rates inevitably trigger elemental segregation and abnormal grain coarsening, challenging the precise compositional and structural control [21]. These limiting features can be solved through the Joule-heating approach, which enables ultrafast material synthesis within seconds under high-intensity pulsed currents [22]. Such an instantaneous high-temperature process facilitates rapid nucleation while suppressing grain growth, yielding ultrafine crystallites with densely packed grain boundaries. Additionally, the transient thermal exposure effectively inhibits elemental diffusion and segregation to yield homogeneous multi-component solid solutions. The non-equilibrium cooling process also stabilizes metastable defect configurations, such as oxygen vacancies and dislocations, to prevent the formation of thermodynamically unfavorable

phases. In turn, the precise modulation of NFs' electronic structures by the Joule-heating approach significantly enhances EMW-absorption performance [23]. Nevertheless, to the best of our knowledge, the synthesis of HESF NFs via Joule-heating for EMW absorption applications has not yet been investigated.

Herein, a novel entropy-driven defect engineering strategy was developed to boost EMW attenuation in spinel ferrites. Based on the conventional $ZnFe_2O_4$, novel $(Mn_{0.2}Co_{0.2}Ni_{0.2}Cu_{0.2}Zn_{0.2})Fe_2O_4$ HESF NFs were prepared by electrospinning coupled with ultrafast Joule-heating technology to leverage the configurational entropy stabilization and induce severe lattice distortions, ultrahigh-density grain boundaries, and abundant oxygen vacancies. The results suggest that the formation of microstructural defects synergistically enhances interfacial/dipole polarization and carrier migration, while the 1D NFs architecture extends EMW propagation paths through a conductive network-enabled multiple scattering mechanism. These features endow the resultant HESF NFs with advanced EMW performances, achieving a record-breaking RL_{min} of -53.58 dB at 1.6 mm and an ultra-wide EAB of 7.82 GHz at 2.03 mm. The composites also exhibit superior radar cross-section (RCS) reduction (35.8 $dB \cdot m^2$) and benchmark metrics in terms of specific effective absorption bandwidth (SEAB), specific reflection loss (SRL), and specific reflection loss and bandwidth (SRLB), surpassing their low-entropy counterparts and state-of-the-art ferrite-based absorbers. Overall, the established paradigm for defect-mediated polarization engineering has potential for fabricating high-entropy architectures for advanced EMW absorption.

2 Experimental section

2.1 Raw Materials

All chemical reagents were of analytical grade and used as received without further purification. Metal nitrate precursors, including $Fe(NO_3)_3 \cdot 9H_2O$, $Zn(NO_3)_2 \cdot 6H_2O$, $Mn(NO_3)_2 \cdot 4H_2O$, $Co(NO_3)_2 \cdot 6H_2O$, $Ni(NO_3)_2 \cdot 6H_2O$, and $Cu(NO_3)_2 \cdot 3H_2O$ were purchased from InnoChem Science &

Technology Co., Ltd. (Beijing, China). Polyacrylonitrile (PAN, 150000 g mol^{-1}, 99.9%) and *N,N*-dimethylformamide (DMF, anhydrous, 99.9%) were received from Aladdin Chemical Reagent Co., Ltd. (Shanghai, China).

2.2 Sample Preparation

High-entropy $(Mn_{0.2}Co_{0.2}Ni_{0.2}Cu_{0.2}Zn_{0.2})Fe_2O_4$ nanofibers were synthesized via electrospinning and Joule heating methods. Initially, 0.7 g of PAN was dissolved in 10 mL DMF under continuous stirring at 60 °C for 3 h to form a stable solution. Subsequently, 2 mmol of $Fe(NO_3)_3·9H_2O$ and 0.2 mmol of $Zn(NO_3)_2·6H_2O$, $Mn(NO_3)_2·4H_2O$, $Co(NO_3)_2·6H_2O$, $Ni(NO_3)_2·6H_2O$, and $Cu(NO_3)_2·3H_2O$ each were added to the above solution and vigorously stirred for another 4 h. The obtained transparent precursor solution was transferred into a 20 mL syringe with a 22-gauge needle, and pristine nanofibers were prepared via electrospinning of the solution under a high voltage of 15 kV, solution supply rate of 0.25 mL h^{-1}, humidity of 40%, and receiving distance of 20 cm.

The Joule heating step was accomplished by first cutting the as-fabricated nanofibrous membranes into 8 cm × 4 cm rectangular specimens, followed by assembly within a copper-electrode-connected carbon felt in a custom-built Joule thermal reactor [24]. Before calcination, the reaction chamber was subjected to three-cycle high-purity argon purging to establish an oxygen-deficient atmosphere. A precise sintering temperature control at ~700 °C was achieved by modulating the input parameters (50 V, 15 A) through a programmable DC power supply (EA, P91000, Germany), with real-time thermal monitoring implemented via an infrared radiation thermometer (Fluke, E1RH-R59, USA). The $(Mn_{0.2}Co_{0.2}Ni_{0.2}Cu_{0.2}Zn_{0.2})Fe_2O_4$ nanofibers were synthesized through an ultrarapid Joule-heating process within 30 s. For comparison, $ZnFe_2O_4$ and $(Mn_{1/3}Co_{1/3}Zn_{1/3})Fe_2O_4$ nanofibers were fabricated using the same protocols.

2.3 Characterization

The phase compositions of the nanofibers were identified by X-ray diffraction (XRD, Bruker AXS D8 Advance, Germany) with Cu Kα radiation, and the results were refined using GSAS Rietveld

software. The elemental chemical states of the nanofibers were determined by X-ray photoelectron spectroscopy (XPS, Axis Ultra DLD, UK). The vacancies were detected by electron paramagnetic resonance (EPR, Bruker EMXplus, Germany) spectrometry. The morphologies were investigated by field-emission scanning electron microscopy (FE-SEM, FEI Quanta 450, USA) and transmission electron microscopy (TEM, JEOL 1400Flash, Japan). Further morphology and structural characterizations related to the uniformity of the elemental distribution were performed by atomic-resolution high-angle annular dark-field scanning TEM (HAADF-STEM) imaging coupled with energy-dispersive X-ray spectroscopy (EDS) elemental mapping using an aberration-corrected STEM (JEOL, JED2300). The lattice strain distributions derived from HAADF-STEM images were quantitatively analyzed using a commercial Geometric Phase Analysis (GPA) software suite. The magnetic properties of nanofibers were analyzed by vibrating sample magnetometry (VSM, Lakeshore 7404, USA).

The relatively complex permittivity and permeability were measured by first grounding fibrous samples into fine powders, followed by uniform blending with paraffin matrix at a mass ratio of 4:6. The mixture was subsequently cold-pressed into toroidal specimens with precise dimensions (inner diameter 3.04 mm, outer diameter 7.00 mm, thickness 2.00 mm). The relative complex permittivity ($\varepsilon_r = \varepsilon' - j\varepsilon''$) and permeability ($\mu_r = \mu' - j\mu''$) were then systematically measured across a 2-18 GHz frequency range using a vector network analyzer (VNA, AV3656D, China) under ambient conditions. The microwave attenuation performances were evaluated by calculating the reflection loss (RL) characteristics based on Eq. (S2) according to the transmission line theory [12]. The effective absorption bandwidth (EAB) was determined at RL reaching below -10 dB within a specific frequency range, corresponding to 90% electromagnetic wave attenuation.

The radar cross-section (RCS) values were simulated using CST Studio Suite 2022. The dielectric loss mechanisms, including conductive loss and polarization loss, were quantitatively decoupled through Python-based numerical analysis. The oxygen vacancy-induced variations in the electrical

properties of samples were evaluated by density functional theory (DFT) calculations, and specific details are provided in the Electronic Supplementary Material (ESM).

3 Results and discussion

3.1 Design and fabrication

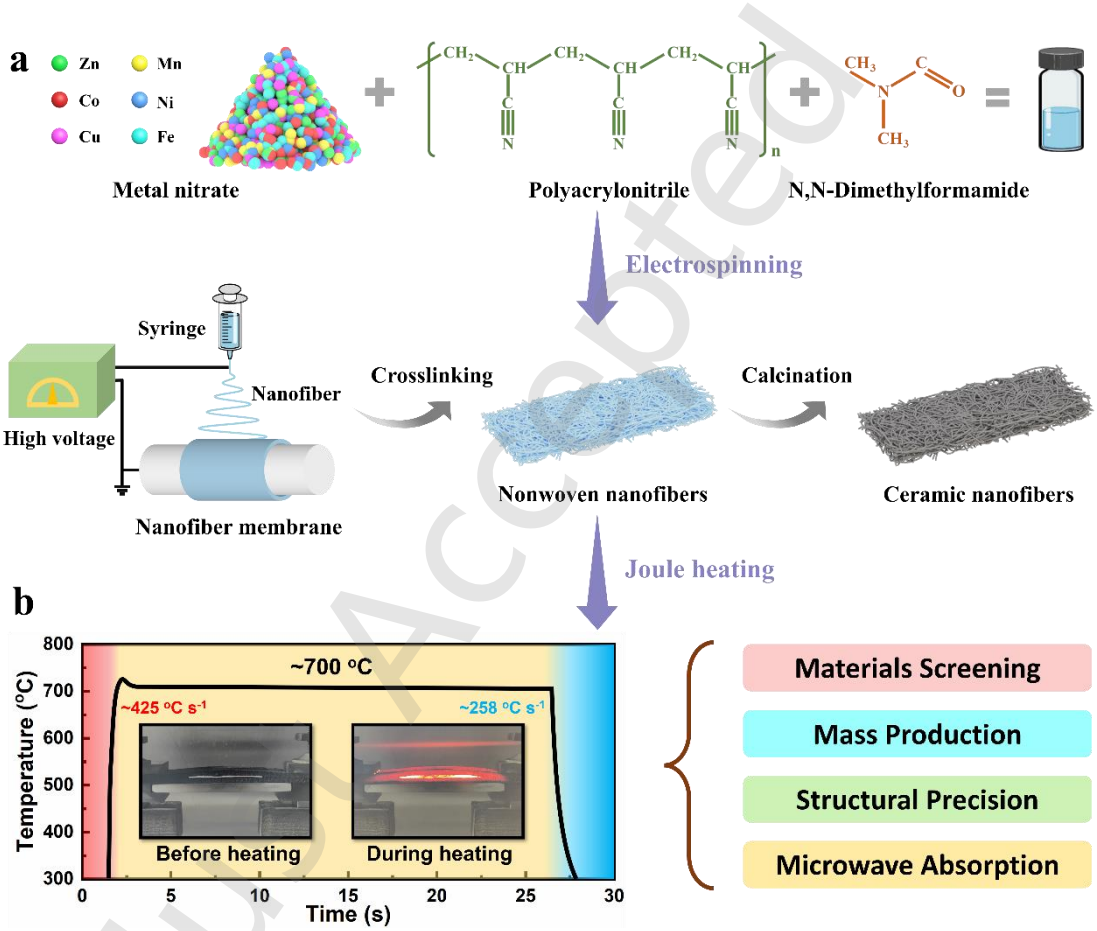

Fig. 1. (a) Schematic representation of the preparation process of HESF NFs by electrostatic spinning and the Joule-heating method. (b) The temperature profile of the Joule-heating process. The insert pattern shows digital images before and during Joule-heating.

The fabrication strategy of HESF NFs is shown in Fig. 1. Briefly, a sol-gel electrospinning process based on metal nitrate as precursors and polyacrylonitrile (PAN) as a continuous polymeric matrix dissolved in polar *N,N*-dimethylformamide (DMF) was utilized to form a homogeneous coordination system. Conventional $ZnFe_2O_4$ with a stable spinel structure was employed as a control to establish

baseline performance metrics. A HE strategy was then implemented to incorporate metal cations (Co, Ni, Mn, and Cu) into the $ZnFe_2O_4$-based spinel ferrite and form NF membranes through the electrospinning method. These constituent elements were strategically selected based on their properties. For instance, Co and Ni ions as typical ferromagnetic components could enhance magnetic loss in EMW absorption, while Cu and Mn ions could favorably contribute to the dielectric properties modulating the dielectric loss of the composites. The minor thermodynamic differences among these elements further facilitate the formation of a stable solid solution.

The Joule-heating process used for the synthesis of the NF membrane is illustrated in Fig. 1b. Within 2 s of the process, the Joule-heating system rapidly attains 700 °C at a rate of approximately 425 °C/s. The system maintains this temperature for ~25 s and subsequently cools down to ambient conditions at 258 °C/s within 4 s. The robust skeleton of the precursor PAN allows the resultant spinel constituents to adopt a uniaxial fibrous alignment. Concurrently, the PAN undergoes carbonization, ultimately yielding HESF NFs. Fig. 1b also suggests significant application potential in materials screening, mass production, and structural precision control, with exceptional promise in EMW absorption. Based on the developed Joule-heating methodology, a series of HE materials, including oxides, borides, and alloys, were synthesized, and their properties in EMW absorption applications were examined along with their multifaceted wave dissipation mechanisms and synergistic multi-element interactions.

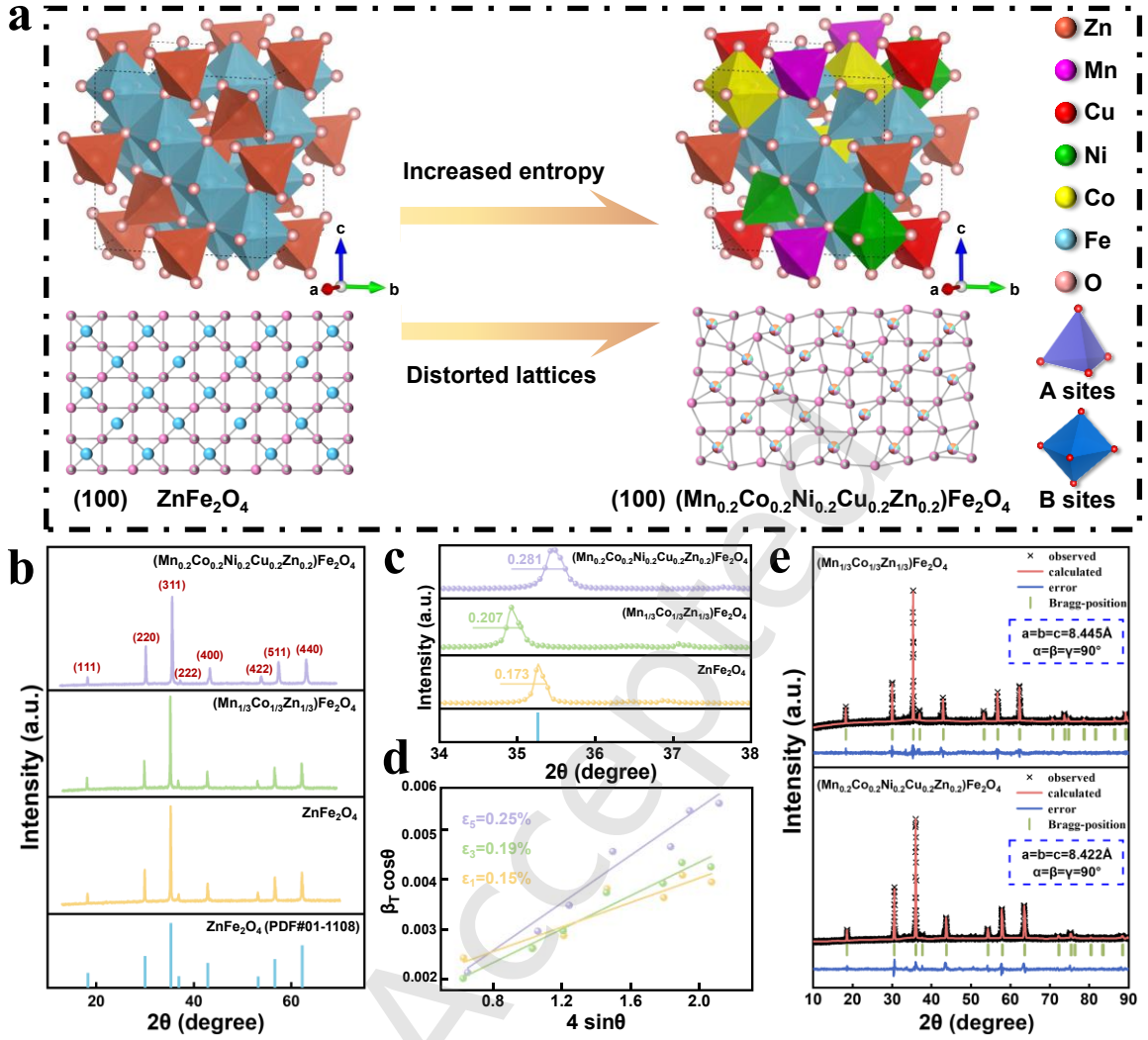

Fig. 2. (a) Crystal structures of HESF and schematic illustration of the distorted lattices in HESF with increased entropy. (b) XRD patterns of the synthesized $ZnFe_2O_4$, $(Mn_{1/3}Co_{1/3}Zn_{1/3})Fe_2O_4$, and $(Mn_{0.2}Co_{0.2}Ni_{0.2}Cu_{0.2}Zn_{0.2})Fe_2O_4$. (c) Enlarged (311) peaks of powder XRD results for (b). (d) Lattice strains quantified by Williamson-Hall analysis. (e) Rietveld refinements of the $(Mn_{1/3}Co_{1/3}Zn_{1/3})Fe_2O_4$ and $(Mn_{0.2}Co_{0.2}Ni_{0.2}Cu_{0.2}Zn_{0.2})Fe_2O_4$.

Following the rapid Joule heating process, entropy-driven metal ions would achieve statistically random lattice occupation, while divalent cations would preferentially occupy A sites (tetrahedral sites) and trivalent cations would inhabit B sites (octahedral sites) [25]. The ideal configurational entropy of the cation sublattice elevates monotonically from 0 for unary $ZnFe_2O_4$, to 1.10*R* for ternary $(Mn_{1/3}Co_{1/3}Zn_{1/3})Fe_2O_4$ (medium-entropy), and reaches 1.61*R* for quinary HESF NFs (high-

entropy). As shown in Fig. 2a, progressive entropy elevation subsequently manifests as distorted lattices within the host material. The crystal structures of the synthesized NFs investigated by X-ray diffraction (XRD, Fig. 2b) show the dominant characteristic peaks of all samples aligning well with the standard PDF card (#01-1108) of $ZnFe_2O_4$ spinel ferrite, with no detectable impurity phases, confirming formation of solid solutions of multiple metal cations within the lattices. The variations in electronegativity and effective cation radius of doped atoms, namely Mn^{2+} (0.66 Å), Co^{2+} (0.58 Å), Ni^{2+} (0.55 Å), Cu^{2+} (0.57 Å), and Zn^{2+} (0.6 Å), result in lattice contraction or expansion [26]. Specifically, the partial substitution of Zn by Mn and Co ions shifts the (311) diffraction peak toward lower angles, whereas co-doping with smaller Ni and Cu ions moves the peak toward higher angles (Fig. 2c). Concurrently, the peak corresponding to the (311) plane undergoes progressive broadening from low-entropy $ZnFe_2O_4$ to high-entropy $(Mn_{0.2}Co_{0.2}Ni_{0.2}Cu_{0.2}Zn_{0.2})Fe_2O_4$ (Fig. 2c), indicative of enhanced internal lattice microstrain. The lattice microstrains quantified through Williamson–Hall analysis (Eq. S1 in the ESM) using peak positions and full width at half maximum (FWHM) of the XRD diffraction peaks demonstrate an increase in microstrain from 0.15% in $ZnFe_2O_4$ to 0.25% in $(Mn_{0.2}Co_{0.2}Ni_{0.2}Cu_{0.2}Zn_{0.2})Fe_2O_4$. In turn, the enhanced entropy significantly aggravates lattice microstrain, as evidenced by Fig. 2d. The Rietveld refinements of XRD patterns in Fig. 2e and Fig. S1 in the ESM confirm the formation of cubic spinel (Fd-3m) structures in all NFs samples, with low reliability factors (R_{wp} < 5.0%, R_p < 3.6%, and χ^2 < 1.50, Table S1 in the ESM) confirming the high fidelity of the refined crystal models. The obtained lattice parameters correlate well with the ionic radii evolution across specimens. For instance, $ZnFe_2O_4$ exhibits lattice parameters $a = b = c$ = 8.436 Å, whereas $(Mn_{1/3}Co_{1/3}Zn_{1/3})Fe_2O_4$ shows increased $a = b = c$ = 8.445 Å, confirming lattice expansion after the incorporation of Mn and Co ions. Conversely, the addition of Cu and Ni ions in $(Mn_{0.2}Co_{0.2}Ni_{0.2}Cu_{0.2}Zn_{0.2})Fe_2O_4$ results in lattice shrinkage with $a = b = c$ = 8.422 Å. Collectively, these results suggest possible lattice distortion within the HESF NFs, warranting further verification through various microstructural characterizations.

The surface elemental compositions and chemical bondings of synthesized $ZnFe_2O_4$-based NFs were analyzed by X-ray photoelectron spectroscopy (XPS). Obviously, the high-resolution XPS spectra in Figs. S2-S3 confirm the presence of bonding associated with Fe-O (711.3 and 724.8 eV for Fe $2p_{3/2}$ and Fe $2p_{1/2}$, respectively), Zn-O (1021.4 and 1044.6 eV for Zn $2p_{3/2}$ and Zn $2p_{1/2}$, respectively), Mn-O (641.7 and 653.3 eV for Mn $2p_{3/2}$ and Mn $2p_{1/2}$, respectively), Ni-O (855.2 and 872.4 eV for Ni $2p_{3/2}$ and Ni $2p_{1/2}$, respectively), Co-O (780.8 and 795.9 eV for Co $2p_{3/2}$ and Co $2p_{1/2}$, respectively), and Cu-O (934.1 and 954.2 eV for Cu $2p_{3/2}$ and Cu $2p_{1/2}$, respectively). Notably, Fe, Co, and Ni exhibit mixed valence states of 2+ and 3+, while other cations exclusively adopt a 2+ oxidation state. Consequently, B sites are predominantly occupied by Fe, Co, and Ni, whereas the remaining metallic elements include partial Fe, Co, and Ni co-occupying A sites. Furthermore, the incorporation of trivalent Co^{3+} and Ni^{3+} in HESF NFs inevitably occupies B sites originally dominated by Fe in $ZnFe_2O_4$, resulting in a diminished peak intensity of Fe^{3+} when compared to Fe^{2+} (Fig. S2). Notably, despite achieving highly homogeneous elemental distribution in HESF NFs, all cations manifest partial atomic ordering at cationic lattice sites governed by electronic configurations of constituent metals [27]. However, the precise quantification of cation distribution across A/B sites and subsequent determination of the chemical formula remain challenging due to the semi-quantitative nature of XPS analysis and potential internal redox reactions among metallic constituents. As illustrated in Fig. S4, the O 1s spectrum comprises three primary components, namely lattice oxygen (O_L), oxygen vacancy (O_V), and surface-adsorbed oxygen (O_S). From Table S2, the calculated area ratios demonstrate a substantial increase in oxygen vacancy contribution from 18.5% in $ZnFe_2O_4$ to 38.7% in $(Mn_{0.2}Co_{0.2}Ni_{0.2}Cu_{0.2}Zn_{0.2})Fe_2O_4$, indicating an enhancement in oxygen vacancy concentration as a function of the increase in entropy.

The unpaired electrons in the synthesized materials were examined by electron paramagnetic resonance (EPR), characterizing their distinctive *g*-factors ($g = 2.003$) to delve into oxygen vacancies within NFs. As shown in Fig. S5, the significantly amplified EPR signal intensity in

$(Mn_{0.2}Co_{0.2}Ni_{0.2}Cu_{0.2}Zn_{0.2})Fe_2O_4$ compared to $(Mn_{1/3}Co_{1/3}Zn_{1/3})Fe_2O_4$ and $ZnFe_2O_4$ confirms greater oxygen vacancy density in HESF NFs, consistent with the XPS analysis. Collectively, these findings demonstrate the successful fabrication of HESF NFs. Notably, the heterometallic doping induces lattice distortion and abundant oxygen vacancies within the HE architecture, conducive to enhancing charge migration under alternating electromagnetic fields for promoted attenuation of EMW through dielectric loss optimization.

3.2 Microstructural characterization

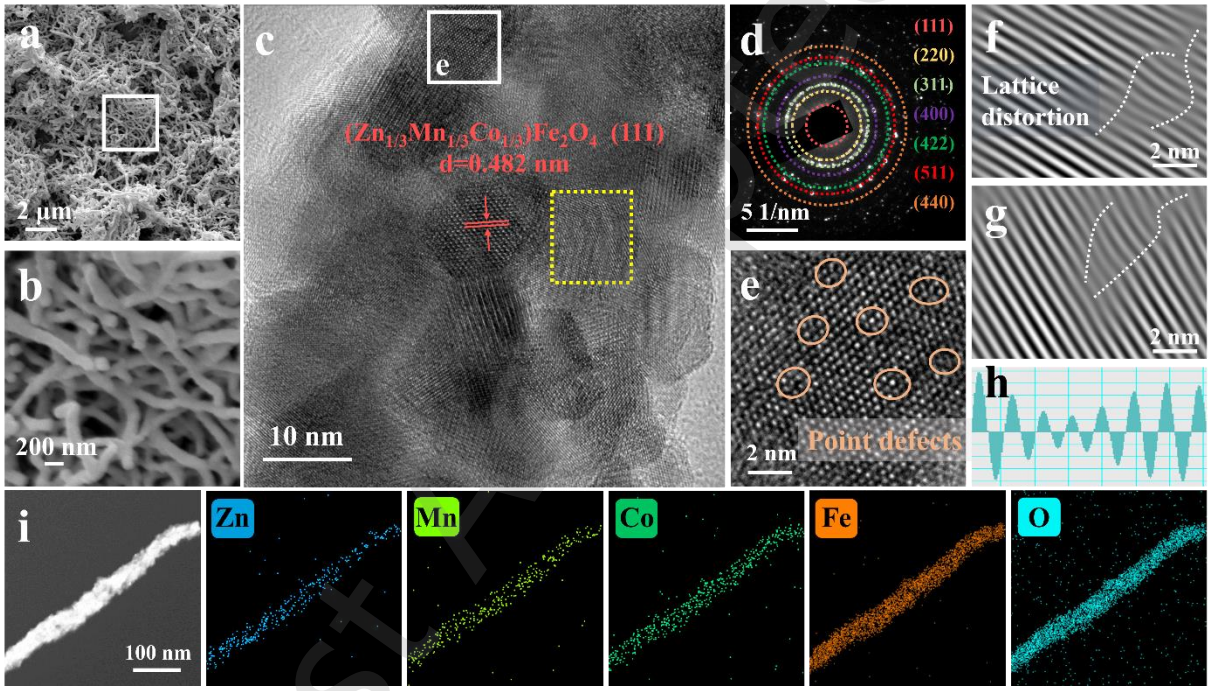

Fig. 3. Morphological and structural characterization of $(Zn_{1/3}Mn_{1/3}Co_{1/3})Fe_2O_4$ NFs. (a, b) SEM imaging, (c) HRTEM imaging, and (d) the corresponding SAED pattern of $(Zn_{1/3}Mn_{1/3}Co_{1/3})Fe_2O_4$. (e) Partial enlarged image of (c). (f, g) Inverse FFT filtered images of the area enclosed by the yellow dashed line in (c). (h) D-spacing of the lattice planes in (g). (i) HADDF-STEM and the corresponding elemental mapping images of $(Zn_{1/3}Mn_{1/3}Co_{1/3})Fe_2O_4$.

Further morphological and structural evolution of the NFs was elucidated by scanning electron microscopy (SEM) and transmission electron microscopy (TEM). As depicted in Fig. S6, the electrospun mats comprising metal salts and PAN exhibit smooth surfaces with uniform 1D fiber

diameters of 200-300 nm, interlinked, and maintain structural integrity. After thermal treatment, the Joule heating-induced polymer pyrolysis slightly fragments the fiber to yield surficial roughness through thermal contraction (Figs. S7a-b, 3a-b, and 4a-b). Nevertheless, the annealed NFs retain significantly higher aspect ratios than the nanoparticle counterparts. Such intertwined and stacked NFs may serve as conduits for electron transfer, forming a 3D conductive network conducive to advanced EMW transmission and enhanced conductive loss [28].

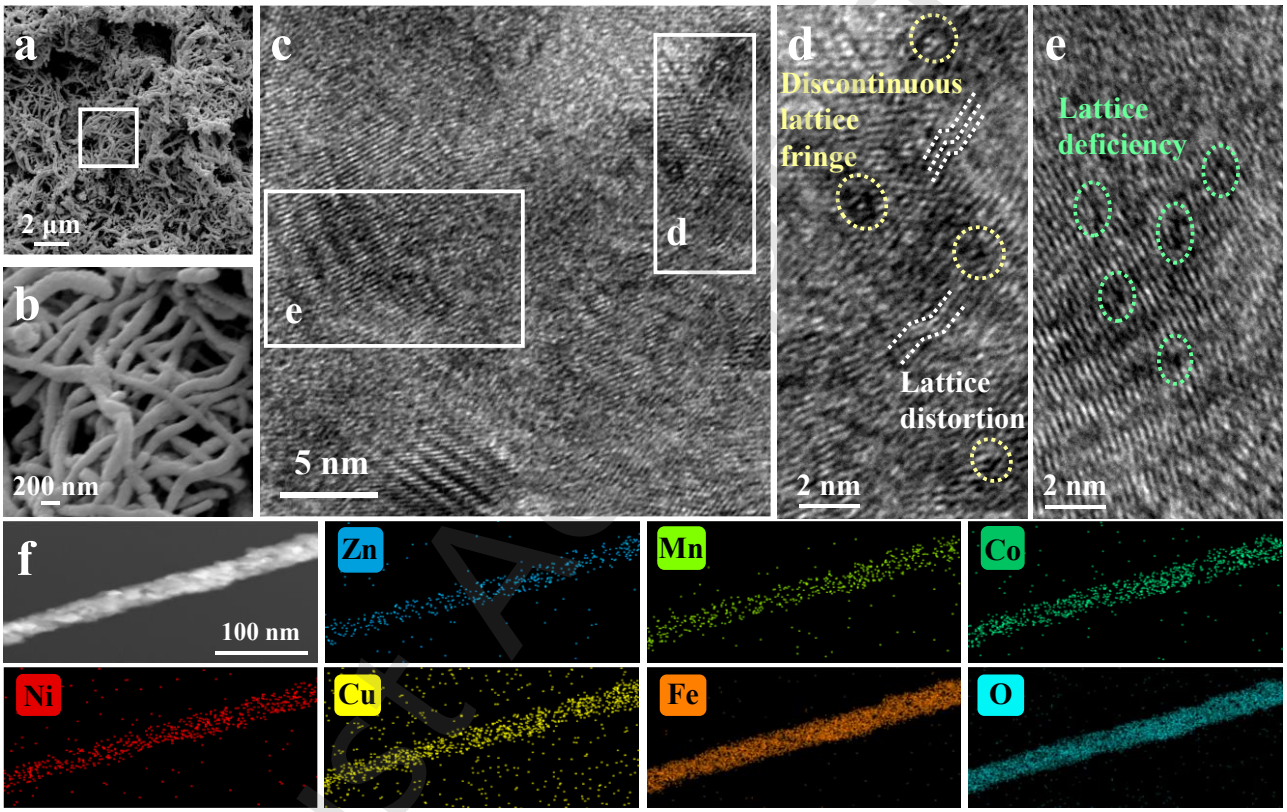

Fig. 4. Morphological and structural characterization of $(Mn_{0.2}Co_{0.2}Ni_{0.2}Cu_{0.2}Zn_{0.2})Fe_2O_4$ NFs. (a, b) SEM images and (c) HRTEM image of $(Mn_{0.2}Co_{0.2}Ni_{0.2}Cu_{0.2}Zn_{0.2})Fe_2O_4$. (d, e) Partial enlarged image of (c). (f) HADDF-STEM and the corresponding elemental mapping images of $(Mn_{0.2}Co_{0.2}Ni_{0.2}Cu_{0.2}Zn_{0.2})Fe_2O_4$.

Further characterization was performed by the high-resolution TEM (HRTEM) technique. As displayed in Fig. S7c, well-defined lattice fringes with a 0.30 nm interplanar spacing are recorded and indexed to the (220) crystallographic plane of $ZnFe_2O_4$. Concurrent high-angle annular dark-

field STEM (HAADF-STEM) imaging and elemental mapping demonstrate homogeneously distributed Zn, Fe, and O species (Fig. S7d). The HRTEM imaging in Fig. 3c indicates the formation of a polycrystalline architecture within $(Mn_{1/3}Co_{1/3}Zn_{1/3})Fe_2O_4$ NFs, with random crystallographic orientations. An obvious lattice spacing of 0.482 nm can also be detected within individual crystallites, indexed to the (111) plane of the $(Mn_{1/3}Co_{1/3}Zn_{1/3})Fe_2O_4$. The selected-area electron diffraction (SAED) pattern further corroborates the formation of polycrystallinity, with concentric rings assigned to the (111), (220), (311), (400), (422), (511), and (440) planes, aligning well with prior XRD analyses. The magnified HRTEM micrograph in Fig. 3e identifies abundant point defects within grains, while the inverse fast Fourier transform (IFFT, Fig. 3f-h) imaging corroborates existing lattice distortions. As evidenced by Fig. 3i, a total of five constituent elements (Zn, Mn, Co, Fe, and O) are uniformly distributed throughout NFs without detectable elemental segregation. For the $(Mn_{0.2}Co_{0.2}Ni_{0.2}Cu_{0.2}Zn_{0.2})Fe_2O_4$ HESF NFs, structural imperfections, such as lattice distortions, discontinuous lattice fringes, and lattice deficiencies, are visible throughout the HRTEM images (Fig. 4c-e), validating the entropy-driven lattice strain mechanism via atomic co-doping. The quantitative elemental composition of the HESF NFs was strictly validated via TEM-EDS analysis (Table S3 in the ESM). The measured total atomic percentages are approximately 2.81 at% Mn, 2.90 at% Co, 2.83 at% Ni, 2.87 at% Cu, 2.87 at% Zn, 28.72 at% Fe, and 57.00 at% O, which strictly matches the ideal AB_2O_4 spinel ferrite stoichiometry while self-consistently reflecting the slight oxygen deficiency (oxygen vacancies, $O_{3.969}$) identified by XPS and EPR. Furthermore, spatially isotropic distribution of all constituent elements in Fig. 4f corroborates the successful synthesis of a single-phase entropy-stabilized configuration in HESF NFs, validating the atomic-scale mixing efficacy through elemental homogeneity. Such ultra-dense polycrystalline grain boundaries and defects are expected to prompt polarization loss mechanisms for boosting microwave dissipation.

3.3 Electromagnetic wave absorption performance

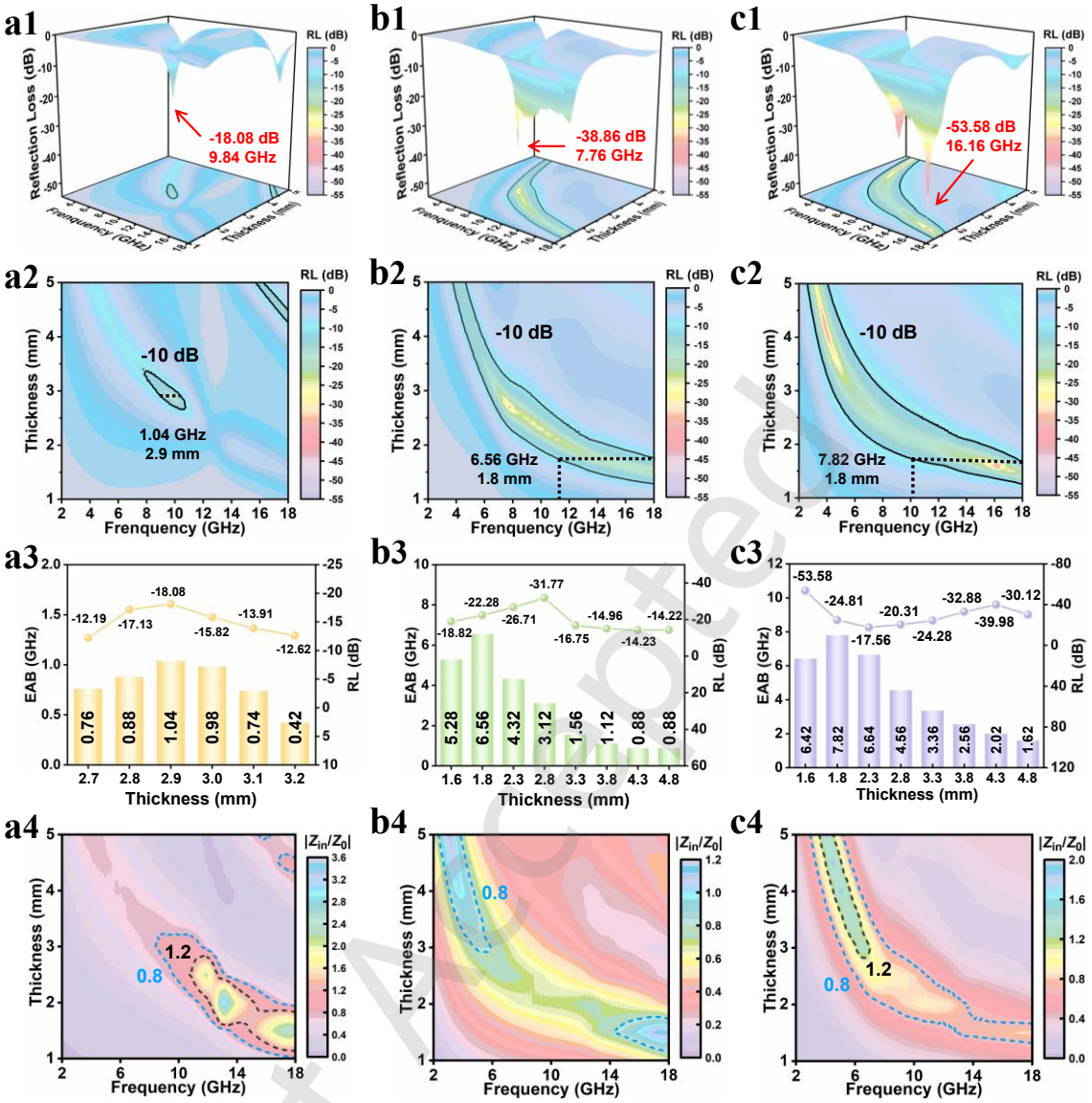

Fig. 5. EMW absorption performances of (a) $ZnFe_2O_4$, (b) $(Mn_{1/3}Co_{1/3}Zn_{1/3})Fe_2O_4$, and (c) $(Mn_{0.2}Co_{0.2}Ni_{0.2}Cu_{0.2}Zn_{0.2})Fe_2O_4$ NFs. (a1-c1) 3D plots and (a2-c2) 2D contours of RL values as a function of frequency and sample thickness. (a3-c3) Summary of RL_{min} and maximum EAB. (a4-c4) 2D map of impedance matching.

The EMW absorption performances of $ZnFe_2O_4$, $(Mn_{1/3}Co_{1/3}Zn_{1/3})Fe_2O_4$, and $(Mn_{0.2}Co_{0.2}Ni_{0.2}Cu_{0.2}Zn_{0.2})Fe_2O_4$ NFs are compared in Fig. 5. The 3D plots and 2D contour plots of RL reveal progressively enhanced attenuation capabilities, primarily attributed to the increased entropy configuration within the materials. As depicted in Fig. 5a, pristine $ZnFe_2O_4$ exhibits inferior EMW absorption properties than its doped counterparts, with an RL_{min} of merely -18.08 dB at 9.84

GHz and a narrow EAB of 1.04 GHz at a matching thickness of 1.9 mm. This deficiency stems from the suboptimal impedance-matching characteristics and an intrinsically limited singular attenuation mechanism. Upon the introduction of Mn and Co co-doping, a marked improvement is observed in RL, EAB, and impedance matching (Fig. 5b). The $(Mn_{1/3}Co_{1/3}Zn_{1/3})Fe_2O_4$ sample achieves a significantly lower RL_{min} of -38.86 dB. Decreasing the $(Mn_{1/3}Co_{1/3}Zn_{1/3})Fe_2O_4$ thickness to 1.8 mm optimizes the EAB to reach an impressive 6.56 GHz. Benefiting from the unique HE structural configuration, the HESF NFs samples exhibit superior overall EMW absorption performances. At an ultra-thin thickness of 1.6 mm (Fig. 5c), the HESF NFs achieve a maximum RL_{min} of -53.58 dB, coupled with an exceptional EAB of 7.82 GHz at a material thickness of only 2.03 mm. Comparative analysis of the 2D impedance contour plots reveals HESF NFs possessing the largest area within the optimal range of 0.8-1.2, signifying superior impedance matching characteristics when compared to $ZnFe_2O_4$ and $(Mn_{1/3}Co_{1/3}Zn_{1/3})Fe_2O_4$. At a thickness of 1.8 mm, the expanded EAB of the HESF NFs effectively covers the entire Ku-band and approximately half of the X-band. At a thickness of 2.0 mm, complete absorption can be achieved over the X-band. Such a remarkable capability to achieve broadband absorption encompassing the entire Ku-band and X-band at specific and relatively thin thicknesses underscores the significant potential of the HESF NFs as highly promising materials for advanced, high-performance EMW management applications.

The EMW attenuation performances of synthesized NFs were assessed through complex permittivity and permeability measurements, where the real permittivity component (ε') facilitates energy storage through polarization mechanisms, whereas the imaginary permittivity component (ε'') governs energy dissipation via dielectric relaxation. As evidenced by Fig. S9a-b, ε' ϵ' exhibits a progressive frequency-dependent attenuation, whereas ε'' displays two characteristic resonance peaks near 8-10 GHz and 13-15 GHz. These prominent dielectric fluctuations originate from the synergistic interplay between collective defect-dipole cluster relaxation and 3D fibrous network percolation resonance. Specifically, high-entropy stabilization pins abundant oxygen vacancies and localized

lattice strains, inducing dipole clusters that undergo collective polarization relaxation under high-frequency electromagnetic fields. Meanwhile, the interconnected 1D nanofiber network establishes micro-current loops, triggering geometric conductive resonance when the electromagnetic skin depth matches the characteristic scale of the conductive network. Such a dispersive permittivity response arises from phase-retarded polarization phenomena under high-frequency alternating EM fields [29]. Notably, the entropy engineering strategy profoundly modulates both ε' and ε'' in prepared NFs, with enhanced values recorded for $(Mn_{0.2}Co_{0.2}Ni_{0.2}Cu_{0.2}Zn_{0.2})Fe_2O_4$ HESF NFs in comparison with $ZnFe_2O_4$ and $(Mn_{1/3}Co_{1/3}Zn_{1/3})Fe_2O_4$. These variations indicate distinctive divergence in polarization behavior and conductivity. Under alternating EM fields, the pronounced grain boundaries in HESF NFs intensify localized charge accumulation, thereby driving interfacial polarization for EMW dissipation. Concurrently, lattice defects, such as oxygen-deficient sites and structural distortions, form a dipole moment that enhances dielectric properties through polarization relaxation. In terms of mechanism, the conduction pathway in spinel structures would operate via hopping of electrons between identical trivalent and divalent ions (such as $Fe^{3+} \rightarrow Fe^{2+}$), governed by the Verwey-de Boer mechanism [30]. In turn, the entropy-mediated proliferation of such ion pairs enhances conductivity. Furthermore, interconnected 1D NFs architectures facilitate the formation of a conductive network. Abundant oxygen vacancies and defects in HESF NFs elevate charge carrier mobility, further enhancing the conductivity.

The dielectric loss tangents ($\tan \delta_\varepsilon = \varepsilon''/\varepsilon'$) of NFs are provided in Fig. S9c. Mean values of 0.125, 0.173, and 0.261 are calculated for $ZnFe_2O_4$, $(Mn_{1/3}Co_{1/3}Zn_{1/3})Fe_2O_4$, and $(Mn_{0.2}Co_{0.2}Ni_{0.2}Cu_{0.2}Zn_{0.2})Fe_2O_4$ NFs, respectively. The variation trend establishes a monotonic relationship between entropy elevation and EMW absorption performance. Additionally, Debye relaxation analysis performed through Eq. (S5) elucidates the polarization behavior of the synthesized NFs. The discernible semicircular features in the Cole-Cole plots of HESF NFs (Fig. S10) indicate the occurrence of multiple polarization relaxation processes, such as interface and dipole

polarization, contrasting markedly with $ZnFe_2O_4$ and $(Mn_{1/3}Co_{1/3}Zn_{1/3})Fe_2O_4$. Critically, the entropy-driven augmentation maximizes semicircle radius, indicative of superior dielectric dissipation in $(Mn_{0.2}Co_{0.2}Ni_{0.2}Cu_{0.2}Zn_{0.2})Fe_2O_4$ based HESF NFs. To sum up, the collective contributions from both the intensified polarization loss and superior conductive loss mechanisms (Fig. S11) enhance the dielectric loss performance of $(Mn_{0.2}Co_{0.2}Ni_{0.2}Cu_{0.2}Zn_{0.2})Fe_2O_4$ NFs, endowing them with exceptional EMW attenuation characteristics. Crucially, the elevated configurational entropy creates a unique thermodynamic environment where defect formation energies are substantially lower than those in traditional binary or quaternary counterparts, giving rise to multi-cation synergistic charge-hopping channels that cannot be replicated in lower-entropy systems [14, 17]. The resulting synergy concurrently optimizes dielectric relaxation, magnetic polarization, and impedance matching.

The magnetic properties of the as-prepared NFs were evaluated through complex permeability characterization. As displayed in Fig. S12a-b, the real component (μ') exhibits an overall declining trend for all three specimens, $ZnFe_2O_4$, $(Mn_{1/3}Co_{1/3}Zn_{1/3})Fe_2O_4$, and $(Mn_{0.2}Co_{0.2}Ni_{0.2}Cu_{0.2}Zn_{0.2})Fe_2O_4$ NFs due to natural resonance, resulting in fluctuations within the range of 0.6-1.7. By comparison, the imaginary component (μ'') displays distinct characteristic resonance peaks. Notably, $(Mn_{0.2}Co_{0.2}Ni_{0.2}Cu_{0.2}Zn_{0.2})Fe_2O_4$ NFs demonstrates consistently superior complex permeability relative to $ZnFe_2O_4$ and $(Mn_{1/3}Co_{1/3}Zn_{1/3})Fe_2O_4$, aligning with its superior dielectric constant behavior (Fig. S9). Under external EM fields, these materials undergo not only electric polarization but also magnetic polarization, forming electromagnetic coupling [31]. Critically, this electromagnetic coupling phenomenon correlates intrinsically with the microstructural characteristics of the materials. The high-entropy effect-induced lattice defects in $(Mn_{0.2}Co_{0.2}Ni_{0.2}Cu_{0.2}Zn_{0.2})Fe_2O_4$ based HESF NFs endow them with enhanced electromagnetic coupling, which, in turn, results in complex permeability.

The coercivity (H_c) and saturation magnetization (M_s) curves of the NFs in Fig. S13 reveal well-defined magnetic hysteresis loops for all specimens, confirming their ferromagnetic nature. The M_s

values are recorded as 8.8 emu/g for $ZnFe_2O_4$, 36.2 emu/g for $(Mn_{1/3}Co_{1/3}Zn_{1/3})Fe_2O_4$, and 51.7 emu/g for $(Mn_{0.2}Co_{0.2}Ni_{0.2}Cu_{0.2}Zn_{0.2})Fe_2O_4$, with corresponding H_c of 211.5, 661.2, and 163.8 Oe, respectively. Noticeably, although the $(Mn_{1/3}Co_{1/3}Zn_{1/3})Fe_2O_4$ sample shows a larger enclosed M-H loop area and higher coercive field, static hysteresis loss contributes negligibly in the 2–18 GHz because domain wall displacement cannot keep pace with high-frequency alternating fields. Instead, microwave magnetic loss is governed by dynamic natural resonance and eddy current dissipation. According to Snoek's law, a higher M_s is essential for elevating high-frequency magnetic permeability. The HESF NFs achieve the highest M_s combined with a moderate H_c, yielding superior initial permeability and dynamic magnetic polarization [32]. Such a dual advantage synergistically contributes to the exceptionally low-loss threshold and enhanced magnetic loss performance of HESF NFs.

The dominant magnetic loss mechanisms were elucidated through C_0 curves calculated according to Eq. (S6). The near-constant C_0 values across the 12-18 GHz frequency range in Fig. S14 indicate eddy current losses dominating the magnetic dissipation in this regime. By contrast, pronounced fluctuations in C_0 values are noticed between 2-12 GHz, suggesting coexisting complex loss mechanisms beyond eddy current effects, such as natural resonance, domain wall displacement loss, and hysteresis loss. Across the entire frequency spectrum, the $(Mn_{0.2}Co_{0.2}Ni_{0.2}Cu_{0.2}Zn_{0.2})Fe_2O_4$ based HESF NFs demonstrate the highest magnetic loss tangent ($\tan \delta_\mu = \mu''/\mu'$, Fig. S12c), attributed to their superior magnetic characteristics in comparison with $ZnFe_2O_4$ and $(Mn_{1/3}Co_{1/3}Zn_{1/3})Fe_2O_4$). These characteristics unequivocally signify substantial contributions of the HESF NFs to EMW attenuation through enhanced magnetic loss.

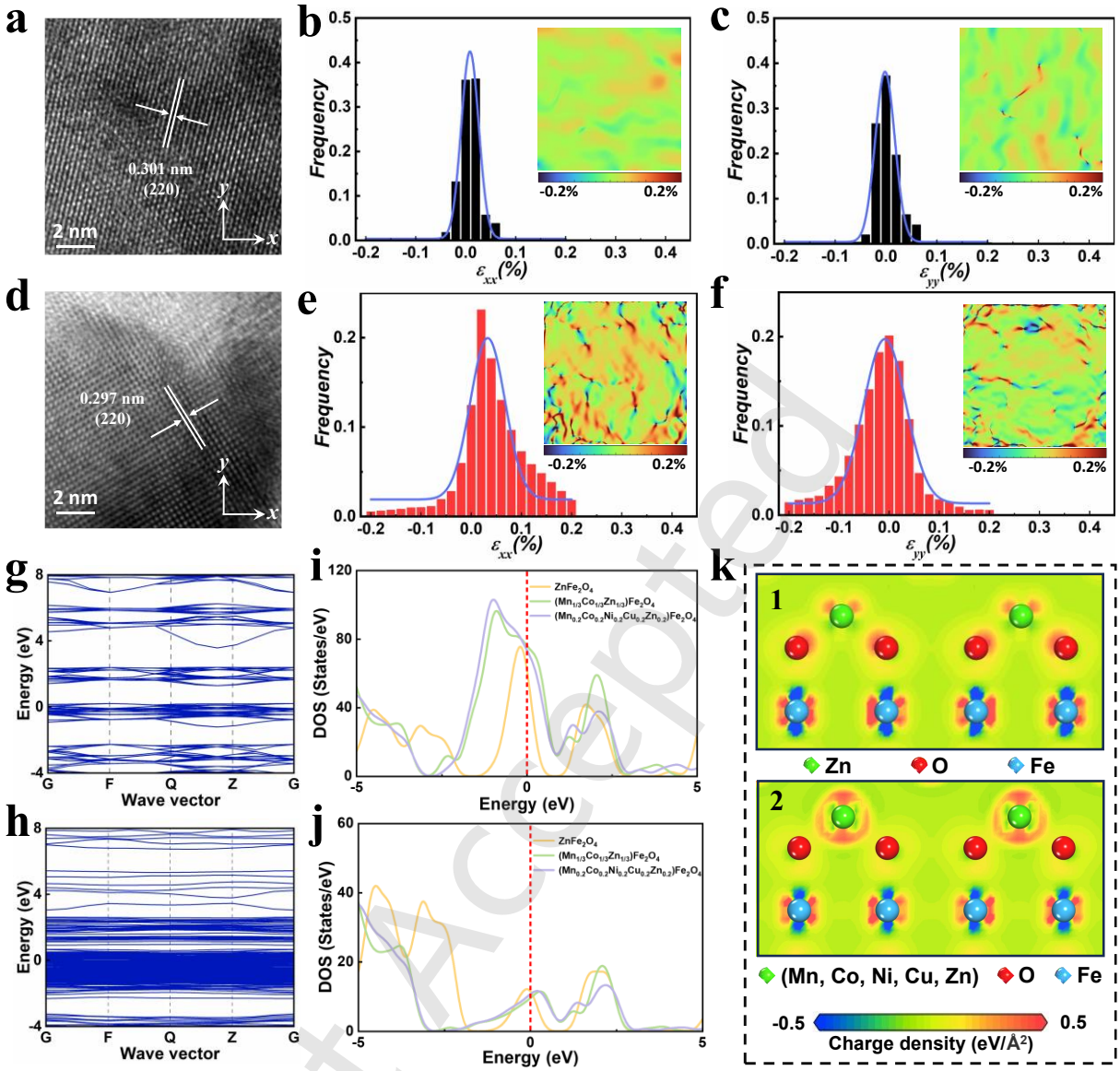

Fig. 6. (a) HRTEM imaging of $ZnFe_2O_4$ NFs and (b, c) corresponding strain distributions along the *xx* (b) and *yy* (c) directions. (d) HRTEM imaging of $(Mn_{0.2}Co_{0.2}Ni_{0.2}Cu_{0.2}Zn_{0.2})Fe_2O_4$ NFs and (e, f) strain distributions along the *xx* (e) and *yy* (f) directions. Band structures of (g) $ZnFe_2O_4$ and (h) $(Mn_{0.2}Co_{0.2}Ni_{0.2}Cu_{0.2}Zn_{0.2})Fe_2O_4$. TDOS (i) and PDOS of O (j) plots for all three NFs. (k) Simulated CDD mappings of NFs. Digits 1 and 2 represent $ZnFe_2O_4$ and $(Mn_{0.2}Co_{0.2}Ni_{0.2}Cu_{0.2}Zn_{0.2})Fe_2O_4$, respectively.

The superior EMW absorption of HESF NFs was confirmed by elucidating the correlation between entropy engineering and lattice strain/oxygen vacancy concentration. The geometric phase analysis (GPA) of HRTEM images in Figs. 6a-f and S15a-c reveals pronounced lattice strain

distribution. Comparative analysis indicates a positive correlation between entropy elevation and amplified lattice strain along ε_{xx} and ε_{yy} directions. Compressive strain (negative values, green-to-black) and tensile strain (positive values, yellow-to-red) are distinctly visualized. To elucidate the intrinsic attenuation mechanisms and decouple the functional roles of structural defects, we systematically evaluated the coupled contributions of high-entropy configurational effects, lattice strain, and oxygen vacancies (Fig. 6 and Fig. S11 in the ESM). Thermodynamically, high configurational entropy accommodates multi-cation ionic radius mismatches, lowering the defect formation energy and stabilizing high-density oxygen vacancies. These vacancies trigger localized unit-cell relaxations that exacerbate macroscopic shear microstrain (Fig. 6e-f). Functionally, despite being intrinsically coupled, lattice strain and oxygen vacancies exhibit complementary dissipation pathways: lattice distortions disrupt local structural inversion symmetry to dictate strain-induced dipole polarization relaxation (ε_p''), whereas oxygen vacancies generate localized in-gap defect states that reduce the activation energy for inter-cation charge hopping, thereby governing conductive dissipation (ε_c'') [33].

First-principles calculations further elucidate the defect-governed dielectric loss mechanisms. As depicted in Figs. 6g-h and S15d, calculated band structures exhibit a progressive narrowing of bandgaps near the Fermi level (E_F) as entropy-driven oxygen vacancy density rises. This creates abundant defect states and band multiplicity near E_F, signifying localized electronic occupation rather than metallic conduction, as confirmed by the total and oxygen-projected density of states (TDOS/PDOS, Fig. 6i-j) [34]. Crucially, the high-entropy lattice distortion induces strong electron scattering that suppresses long-range macroscopic conductivity, thereby averting unwanted surface microwave reflection and preserving impedance matching. Simultaneously, these dense localized defect states lower the activation energy barrier for short-range electron hopping between heterovalent cation pairs (Fe^{2+}/Fe^{3+}, Co^{2+}/Co^{3+}, Ni^{2+}/Ni^{3+}) via the Verwey-de Boer mechanism [35]. Charge density difference (CDD) maps (Figs. 6k and S15e) further reveal expanded, asymmetric

polarization regions surrounding oxygen atoms and vacancy sites. Notably, these DFT findings align seamlessly with multi-scale experimental characterizations to forge a comprehensive micro-to-macro physical framework. Specifically, XPS and EPR results quantify high-density oxygen vacancies and localized unpaired electrons, which work synergistically with the DFT-predicted in-gap states and asymmetric charge centers to dynamically boost localized charge mobility and defect-dipole relaxation. This theoretical-experimental synergy directly rationalizes the measured elevation in ε'', enhanced ε_c'' and ε_p'', and distorted Cole-Cole semicircles.

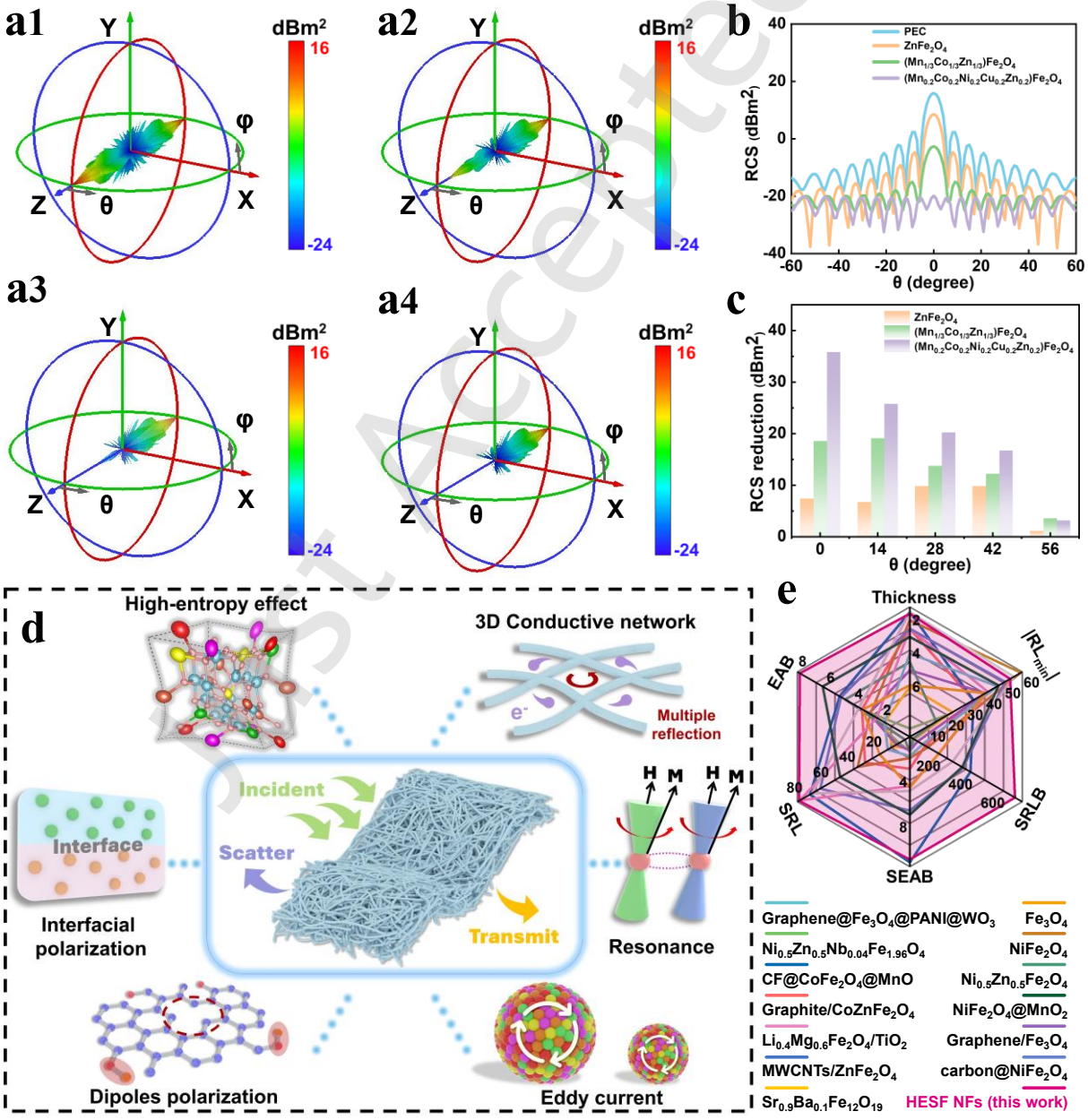

Fig. 7. 3D RCS simulation results of (a1) PEC, (a2) $ZnFe_2O_4$, (a3) $(Mn_{1/3}Co_{1/3}Zn_{1/3})Fe_2O_4$, and (a4) $(Mn_{0.2}Co_{0.2}Ni_{0.2}Cu_{0.2}Zn_{0.2})Fe_2O_4$ NFs. (b) 2D RCS simulation curves of PEC and corresponding NFs at the scattering angle range from -60° to 60°. (c) RCS reduction values of all samples at different scattering angles. (d) Schematic diagram illustrating the EMW attenuation mechanism of HESF NFs. (e) Comparison of EMW absorption performance of the as-prepared HESF NFs with recently published ferrite-based composites.

The EMW absorption under real far-field conditions was assessed through systematic radar cross section (RCS) simulations via CST on perfect electric conductor (PEC) substrates coated with $ZnFe_2O_4$, $(Mn_{1/3}Co_{1/3}Zn_{1/3})Fe_2O_4$, and $(Mn_{0.2}Co_{0.2}Ni_{0.2}Cu_{0.2}Zn_{0.2})Fe_2O_4$ NFs. In Fig. 7a1-a4, the 3D monostatic RCS patterns demonstrate a stark contrast. Notably, the uncoated PEC manifests pronounced reflection, while HESF NFs-coated counterparts exhibit diminished radar wave scattering intensities. The angular-dependent RCS curves (-60° to 60°) in Fig. 7b confirm a progressive RCS reduction from $ZnFe_2O_4$ to HESF systems, aligning well with their intrinsic microwave dissipation properties. Throughout angular scanning domains, the $(Mn_{0.2}Co_{0.2}Ni_{0.2}Cu_{0.2}Zn_{0.2})Fe_2O_4$ NFs based HESF NFs persistently maintain RCS values below -20 $dB{\cdot}m^2$. The quantitative RCS reduction analysis in Fig. 7c further confirms the superior performance of $(Mn_{0.2}Co_{0.2}Ni_{0.2}Cu_{0.2}Zn_{0.2})Fe_2O_4$ based HESF NFs, with a maximum reduction of 35.8 $dB{\cdot}m^2$ recorded at 0° incidence, surpassing those of $ZnFe_2O_4$ and $(Mn_{1/3}Co_{1/3}Zn_{1/3})Fe_2O_4$. These attributes compellingly substantiate the exceptional radar stealth capabilities of $(Mn_{0.2}Co_{0.2}Ni_{0.2}Cu_{0.2}Zn_{0.2})Fe_2O_4$ based HESF NFs and their potential for EM protection applications.

The above exceptional microwave absorption performance of $(Mn_{0.2}Co_{0.2}Ni_{0.2}Cu_{0.2}Zn_{0.2})Fe_2O_4$ based HESF NFs may arise from synergistic mechanisms. First, the HE effect-driven lattice distortion intensifies localized polarization (Fig. 7d), substantially attenuating under EM fields. The ultra-dense crystalline defects serving as polarization centers also activate defect and dipole polarization characteristics. Second, the heterometallic doping creates a charge imbalance at the

material interface due to atomic radius/electronegativity mismatches, while pronounced grain boundaries foster dislocations and stacking faults. These pathways collectively enhance interfacial polarization via charge accumulation and redistribution [36, 37]. Third, the 3D interconnected network not only facilitates carrier migration and hopping for establishing a microcurrent amplification system for conductive loss, but also prolongs EMW propagation through multi-reflection and scattering pathways [38, 39]. Fourth, complementary magnetic loss mechanisms (eddy current/resonance) and dielectric dissipation further elevate attenuation efficiency. All these features result in superior HESF NFs over other reported ferrite-based composite absorbers, as confirmed by the comparative analysis of EMW absorption properties in terms of EAB, RL_{min}, thickness, specific reflection loss (SRL), specific effective absorption bandwidth (SEAB), and specific reflection loss and absorption bandwidth (SRLB) in Fig. 7e and Table S4 [40-52]. The synergistic multifunctional mechanisms endow the $(Mn_{0.2}Co_{0.2}Ni_{0.2}Cu_{0.2}Zn_{0.2})Fe_2O_4$ based HESF NFs with unparalleled integrated performance, highlighting their potential as high-efficiency, lightweight EMW absorption materials for practical applications.

4 Conclusion

In summary, a novel engineered defect-rich $(Mn_{0.2}Co_{0.2}Ni_{0.2}Cu_{0.2}Zn_{0.2})Fe_2O_4$ NFs was designed and successfully prepared through an entropy-driven strategy via electrospinning and ultrafast Joule-heating. The synergistic integration of severe lattice distortions, abundant oxygen vacancies, and ultrahigh-density grain boundaries amplifies dipole and interfacial polarization. The 3D fibrous network architecture inherently boosts conductive loss and promotes EMW multiple scattering, synergistically optimizing the impedance matching characteristics. Defect-induced bandgap narrowing and increased charge redistribution-triggering dielectric loss are confirmed through DFT calculations. All these features result in outstanding EMW absorption performance of HESF NFs, with a RL_{min} of -53.58 dB (1.6 mm), an EAB of 7.82 GHz (2.03 mm), and superior RCS reduction of

35.8 dB·m^2. Overall, the proposed entropy engineering strategy of spinel ferrite-based NFs can be used as a universal strategy to amplify defect-governed polarization, while providing a blueprint for developing advanced EM functional materials through Joule heating suitable for materials screening, mass production, and structural precision control.

Acknowledgements

We would like to thank MogoEdit (https://www.mogoedit.com) for its English editing during the preparation of this manuscript. Also, thanks to eceshi (www.eceshi.com) for the XRD and XPS analysis.

Funding

This research was financially supported by the Young Talent of Lifting engineering for Science and Technology in Shandong (Grant No. SDAST2024QTB030) and Shandong Province Technology Project (M20253905).

Author contributions

Haiming Li: Methodology, Investigation, Data Curation. **Yuhang Bai:** Investigation, Formal analysis, Writing - Original Draft. **Ziying Feng:** Investigation. **Dan Luo:** Data curation, Investigation. **Yudong Gao:** Methodology. **Zexian Xu:** Funding acquisition, Project administration, Resources, Writing - review & editing.

Availability of data and materials

The data that support the findings of this study are available from the corresponding author upon reasonable request.

Competing interests

The authors have no competing interests to declare that are relevant to the content of this article.

Electronic Supplementary Material (ESM)

Supplementary material is available in the online version of this article.

References

[1] Qi Q, Li T, Yang H, et al. Recent advances in structural engineering of ceramic microwave absorption materials: From nano/micro architectures to macroscale design. *J. Adv. Ceram.* 2025, 14: 9221205.

[2] He Y, Liu D, Dou S, et al. Interface-engineered decoupled conductivity and relaxation: Synergistic modulation of Debye-parameters in N-doped SiO_2/MXene broadband wave-absorbing materials. *J. Adv. Ceram.* 2025, 14: 9221150.

[3] Zhang X, Tian X-L, Qin Y, et al. Conductive metal–organic frameworks with tunable dielectric properties for boosting electromagnetic wave absorption. *ACS Nano* 2023, 17: 12510-12518.

[4] Dai G, Deng R, Zhang T, et al. Quantitative evaluation of loss capability for in situ conductive phase enhanced microwave absorption of high-entropy transition metal oxides. *Adv. Funct. Mater.* 2022, 32: 2205325.

[5] Xie X, Wang B, Wang Y, et al. Spinel structured MFe_2O_4 (M = Fe, Co, Ni, Mn, Zn) and their composites for microwave absorption: a review. *Chem. Eng. J.* 2022, 428: 131160.

[6] Huang L, Li J, Wang Z, et al. Microwave absorption enhancement of porous C@$CoFe_2O_4$ nanocomposites derived from eggshell membrane. *Carbon* 2019, 143: 507-516.

[7] Zhao H, Zhang C, Li Y, et al. Ordered cellular 2D/2D biomass-derived carbon nanosheet/MXene aerogels for ultralight and high-performance microwave absorption. *J. Adv. Ceram.* 2025, 14: 9221214.

[8] Wang X, Lu Y, Zhu T, et al. $CoFe_2O_4$/N-doped reduced graphene oxide aerogels for high-performance microwave absorption. *Chem. Eng. J.* 2020, 388: 124317.

[9] Zhang X-J, Wang G-S, Cao W-Q, et al. Enhanced microwave absorption property of reduced graphene oxide (RGO)-$MnFe_2O_4$ nanocomposites and polyvinylidene fluoride. *ACS Appl. Mater. Interfaces* 2014, 6: 7471-7478.

[10] Gai L, Chen Y, Wang Y, et al. Engineering impedance-matched double-shells in hollow Co/carbon microspheres with gradient graphitization for high-efficiency electromagnetic wave absorption. *J. Adv. Ceram.* 2025, 14: 9221212.

[11] Wen Z, Tang Z, Liu Y, et al. Ultrastrong and high thermal insulating porous high-entropy ceramics up to 2000 °C. *Adv. Mater.* 2024, 36: 2311870.

[12] Zhao B, Yan Z, Du Y, et al. High-entropy enhanced microwave attenuation in titanate perovskites. *Adv. Mater.* 2023, 35: 2210243.

[13] Lv S, Jiang Y, Liu M, et al. Vacancy-mediated electromagnetic loss tuning in Cr-doped lanthanum manganite perovskites for broadband and high-intensity microwave absorption. *J. Adv. Ceram.* 2025, 14: 9221202.

[14] Wang S, Ouyang Y, Guo L, et al. Boosting microwave attenuation in high-entropy carbide ceramics via magnetic Co incorporation and microstructural engineering. *J. Adv. Ceram.* 2025, 14: 9221177.

[15] Gu F, Wang W, Meng H, et al. Lattice distortion boosted exceptional electromagnetic wave absorption in high-entropy diborides. *Matter* 2025, 8: 102004.

[16] Luo W, Jiang X, Liu Y, et al. Entropy-driven morphology regulation of MAX phase solid solutions with enhanced microwave absorption and thermal insulation performance. *Small* 2024, 20: 2305453.

[17] Li Y, Zhang M, Chen J, et al. Ceramic-based electromagnetic interference shielding materials: Mechanisms, optimization strategies, and pathways to next-generation applications. *J. Adv. Ceram.* 2025, 14: 9221194.

[18] Li Y, Yuan M, Liu H, et al. In situ synthesis of $CoFe_2O_4$ nanocrystals decorated in mesoporous carbon nanofibers with enhanced electromagnetic performance. *J. Alloys Compd.* 2020, 826: 154147.

[19] Zhu Y, Guan L, Duan C, et al. High-entropy transition metal carbide nanowires with enhanced microwave absorption properties. *J. Mater. Sci. Technol.* 2025, 224: 302-311.

[20] Wei Y, Shi Y, Zhang X, et al. Electrospinning of lightweight TiN fibers with superior microwave absorption. *J. Mater. Sci.: Mater. Electron.* 2019, 30: 14519-14527.

[21] Tian L, Zhang Z, Liu S, et al. High-entropy spinel oxide nanofibers as catalytic sulfur hosts promise the high gravimetric and volumetric capacities for lithium–sulfur batteries. *Energy Environ. Mater.* 2022, 5: 645-654.

[22] Wang C, Ping W, Bai Q, et al. A general method to synthesize and sinter bulk ceramics in seconds. *Science* 2020, 368: 521-526.

[23] Wang S, Liu Q, Li S, et al. Joule-heating-driven synthesis of a honeycomb-like porous carbon nanofiber/high entropy alloy composite as an ultralightweight electromagnetic wave absorber. *ACS Nano* 2024, 18: 5040-5050.

[24] Bai Y, Li J, Lu H, et al. Ultrafast high-temperature sintering of high-entropy oxides with refined microstructure and superior lithium-ion storage performance. *J. Adv. Ceram.* 2023, 12: 1857-1871.

[25] Dong Q, Hong M, Gao J, et al. Rapid synthesis of high-entropy oxide microparticles. *Small* 2022, 18: 2104761.

[26] Shannon R D. Revised effective ionic radii and systematic studies of interatomie distances in halides and chaleogenides. *Acta Cryst.* 1976, 32: 751-767.

[27] Jiang S, Hu T, Gild J, et al. A new class of high-entropy perovskite oxides. *Scr. Mater.* 2018, 142: 116-120.

[28] Wu S, Wang C, Tang Y, et al. Metal–organic framework-derived hierarchical Cu_9S_5/C nanocomposite fibers for enhanced electromagnetic wave absorption. *Adv. Fiber Mater.* 2024, 6: 430-443.

[29] Zhao B, Yan Z, Liu L, et al. A liquid-metal-assisted competitive galvanic reaction strategy toward indium/oxide core−shell nanoparticles with enhanced microwave absorption. *Adv. Funct. Mater.* 2024, 34: 2314008.

[30] Verwey E J W, Heilmann E L. Physical properties and cation arrangement of oxides with spinel structures I. Cation arrangement in spinels. *J. Chem. Phys.* 1947, 15: 174-180.

[31] Huang J, Zeng X, Jiang X, et al. In situ construction of MXene derivatives and rare metal doping in nanofibers for multifunctional and ultrathin electromagnetic responses. *Adv. Funct. Mater.* 2025, e10047.

[32] Tian Z, Hu F, Zhang P, et al. High-entropy engineering of A-site in MAX phases toward superior microwave absorption properties. *Matter* 2025, 102367.

[33] Zhao X, Bai Y, Yang Y, et al. Ultrafast carbothermal shock synthesis of submicron high-entropy carbides: dual enhancement of oxidation resistance and microwave absorption. *Mater. Des.* 2025, 257: 114436.

[34] Quan B, Shi W, Ong S J H, et al. Defect engineering in two common types of dielectric materials for electromagnetic absorption applications. *Adv. Funct. Mater.* 2019, 29: 1901236.

[35] Goldsmid H J. Transport effects in semi-metals and narrow-gap semiconductors. *Adv. Phys.* 1965, 14: 273-326.

[36] Song L, Hu F, Chen Y*, et al.* Heterointerface-Engineered SiC@SiO_2@C Nanofibers for Simultaneous Microwave Absorption and Corrosion Resistance. *Adv. Sci.* 2025, 12: e09071.

[37] Chen Y, Chen M, Lei H*, et al.* Microwave-assisted synthesis of high-performance TaC nanorods for enhanced electromagnetic wave absorption. *J. Adv. Ceram.* 2025, 14: 9221130.

[38] Geng W, Song L, Liu Y*, et al.* Air layer-engineered Cf@void@SiCnf composites for enhanced electromagnetic wave absorption. *Chem. Eng. J.* 2025, 524: 169149.

[39] Guan L, Xu X, Song L*, et al.* Biomass carbon-derived SiC nanowires for efficient electromagnetic wave absorption. *Mater. Today Nano* 2025, 32: 100680.

[40] Wang S, Ren H, Lian W, et al. Purification and dissociation of raw palygorskite through wet ball milling as a carrier to enhance the microwave absorption performance of Fe_3O_4. *Appl. Clay Sci.* 2021, 200: 105915.

[41] Mandal D, Gorai A, Mandal K. Electromagnetic wave trapping in $NiFe_2O_4$ nano-hollow spheres: an efficient microwave absorber. *J. Magn. Magn. Mater.* 2019, 485: 43-48.

[42] Huang X, Zhang J, Lai M, et al. Preparation and microwave absorption mechanisms of the NiZn ferrite nanofibers. *J. Alloys Compd.* 2015, 627: 367-373.

[43] Wang Y, Fu Y, Wu X, et al. Synthesis of hierarchical core-shell $NiFe_2O_4$@MnO_2 composite microspheres decorated graphene nanosheet for enhanced microwave absorption performance. *Ceram. Int.* 2017, 43: 11367-11375.

[44] Wang T, Liu Z, Lu M, et al. Graphene–Fe_3O_4 nanohybrids: synthesis and excellent electromagnetic absorption properties. *J. Appl. Phys.* 2013, 113.

[45] Wang Y, Gao X, Zhou H, et al. Fabrication of biomass-derived carbon decorated with $NiFe_2O_4$ particles for broadband and strong microwave absorption. *Powder Technol.* 2019, 345: 370-378.

[46] Liu J-L, Zhang P, Zhang X-K, et al. Synthesis and microwave absorbing properties of La-doped Sr-hexaferrite nanopowders via sol–gel auto-combustion method. *Rare Met.* 2017, 36: 704-710.

[47] Shu R, Zhang G, Wang X, et al. Fabrication of 3D net-like MWCNTs/$ZnFe_2O_4$ hybrid composites as high-performance electromagnetic wave absorbers. *Chem. Eng. J.* 2018, 337: 242-255.

[48] Bhattacharya P, Hatui G, Mandal A, et al. Investigation of microwave absorption property of the core–shell structured $Li_{0.4}Mg_{0.6}Fe_2O_4/TiO_2$ nanocomposite in X-band region. *J. Alloys Compd.* 2014, 590: 331-340.

[49] Huang X, Zhang J, Rao W, et al. Tunable electromagnetic properties and enhanced microwave absorption ability of flaky graphite/cobalt zinc ferrite composites. *J. Alloys Compd.* 2016, 662: 409-414.

[50] Feng A, Hou T, Jia Z, et al. Synthesis of a hierarchical carbon fiber@cobalt ferrite@manganese dioxide composite and its application as a microwave absorber. *RSC Adv.* 2020, 10: 10510-10518.

[51] Qian K, Yao Z, Lin H, et al. The influence of Nd substitution in Ni–Zn ferrites for the improved microwave absorption properties. *Ceram. Int.* 2020, 46: 227-235.

[52] Wang Y, Wu X, Zhang W, et al. 3D heterostructure of graphene@Fe_3O_4@WO_3@PANI: preparation and excellent microwave absorption performance. *Synth. Met.* 2017, 231: 7-14.